

Experimental verification of the IPI sizing technique

Sebastian Kosch

July 2014

List of symbols and abbreviations

$\Delta\vartheta$	Angular spacing between two adjacent fringes
Δz	Distance along the z -axis between the focal plane of the lens and the light sheet
\hat{N}_{fr}	Peak fringe count measured
χ	Scalar value relating the fringe count N_{fr} to the physical diameter of the particle D_d
D_i	Diameter (in pixels) of the defocussed image
D_{padded}	Width (in pixels) of the padded input to the Fourier transform
D_d	Physical diameter of the particle (here: droplet)
$d_{p,x}; d_{p,y}$	Physical dimensions of a pixel on the camera's CCD sensor
f_{peak}	Peak frequency
M	Magnification
N_{fr}	Number of fringes
s_x	Distance, in pixels, between two adjacent fringes

Introduction

1.1 Why spray sizing is important

1.2 What our contributions in this paper are

- Our contributions: - Pupillary magnification has to be taken into account - Circle detection algorithm is crap

1.3 What other work has been done in this area

Experimental setup

- Our setup:

2.1 Dantec system

- Dantec system

2.2 PDPA system

- TSI system

2.3 Droplet generator

- Droplet generator

2.4 Verification of droplet sizes

This is where I show pictures and tables, showing that the formula actually works.

2.4.1 Colliding droplets

No droplet generation mechanism is perfect. Small fluctuations in flow rate, unwanted harmonic vibrations and air turbulence can cause disturbances in the stream of evenly spaced droplets – the smaller the droplets, the more often this happens. Occasionally, this will lead to the collision of two droplets some distance away from the orifice.

When two drops of diameter D_d collide, the diameter of the new droplet equals

$$D_{d+d} = 2\sqrt[3]{2 \left(\frac{D_d}{2}\right)^3} = \sqrt[3]{2}D_d \approx 1.26D_d. \quad (2.1)$$

Indeed, secondary peaks will often appear in diameter histograms at precisely 126% of the peak diameter. As long as the underlying phenomenon is understood and kept under control, these secondary peaks should be no cause for concern during the calibration. Typically, photographs will confirm that a few droplets go astray and collide with others. Since the “real” diameter peaks are easily discerned, the secondary peaks can simply be ignored.

Interferometric Particle Imaging (IPI)

[Introductory paragraph], saying that this is also called ILIDS (invented by Glover et al. [1])

3.1 Operating principle

The number of fringes N_{fr} appearing in the image has a simple linear relationship to the droplet diametre D_d :

$$N_{\text{fr}} = \kappa D_d, \quad (3.1)$$

where κ is a constant derived from the optical configuration:

$$\kappa = \frac{\arcsin\left(\frac{D_a}{2z}\right)}{\lambda} \left(\cos\frac{\varphi}{2} - \frac{m \sin\frac{\varphi}{2}}{\sqrt{m^2 + 1 - 2m \cos\frac{\varphi}{2}}} \right). \quad (3.2)$$

In the above expression D_a is the aperture diametre, z is the distance of the lens to the laser sheet, φ is the off-axis angle (90 degrees in most setups, including ours), and m is the relative refractive index of the droplets (1.333 for water in air).

As a consequence of geometrical optics, the distance s_x (in pixels) between two adjacent fringes has a linear relationship with the defocussing distance Δz , where M is the magnification, $d_{p,x}$ is the physical size of a camera sensor pixel, and $\Delta\vartheta$ is the angle subtended by two adjacent fringes entering the lens [2]:

$$s_x = \frac{\Delta\vartheta \Delta z}{M d_{p,x}} \quad (3.3)$$

Of course, equation (3.3) is only meaningful where $\Delta z \gg 0$. If the image is (approximately) focussed, fringes will give way to a sharp image of either both glare points or a single bright spot – depending on diffraction effects and the camera’s resolution.

(Fill in more details here.)

3.1.1 Influence of the scattering angle φ

The scattering angle φ determines the relative contribution of different scattering orders of light to the imaged fringe pattern. Both geometric optics [3] and Mie theory provide methods to compute the total scattered intensity for a given φ and m . Some examples can be found in Kawaguchi et al. [4] and Mounaim-Rousselle and Pajot [5]. The geometric analysis approach is not valid beyond $\varphi > 70^\circ$, as the first-order scattered beam ($p = 1$) is not visible from this angle [1].

While authors have identified several forward angles as optimal for their applications, e.g. $\varphi = 45^\circ$ [1] or $\varphi = 66^\circ$ [5], such configurations inevitably result in a variation in z , leading to different degrees of defocussing across the image – unless the camera itself is angled with respect to the lens to correct for this aberration (the so-called *Scheimpflug condition*). Since the latter approach requires specialized optical equipment, $\varphi = 90^\circ$ is used in many setups, including the one in this paper (Section 3.2).

3.1.2 Optical limits on fringe detection

Optics impose theoretical and practical size limits on the droplets to be measured. We will outline them in the following paragraphs; the reader is referred to Damaschke et al. [6] for a more detailed analysis.

Nyquist criterion for the fringe density. The Nyquist criterion requires that for the camera to be able to resolve a pair of neighbouring fringes, they must be at least two pixels apart. This can easily be achieved by sufficiently defocussing the lens, which widens the fringe image, increasing the number of pixels covered by each fringe. The lens mechanics permitting, any arbitrarily large droplet can thus be measured after a quick adjustment. In theory, this correction is effective until the defocussed droplet image is too large for the CCD sensor, and fringes are cut off. In practice, overlap and noise (see below) will cause significant problems long before the image can be defocussed beyond the sensor edges.

Overlapping droplet images. As the lens is brought farther out of focus, the droplet images dilate and overlap one another. Increasing levels of overlap frustrate attempts to identify and analyse the images. Although the slit aperture method discussed in Chapter 4 was developed to circumvent this effect, it is not entirely immune to it – particularly when droplets are very closely spaced, as they often are when vibrating orifice droplet generators are used. See Section 3.3.1 for a more in-depth discussion.

Signal-to-noise ratio. Image noise is a significant source of trouble in IPI analysis – indeed, many droplet images must be discarded as data sources because they are too noisy. Noise affects small droplets in particular because they scatter less light than larger ones,¹ but it is also a problem with deeply out-of-focus images of very large droplets, as dilated droplet images spread the same amount of light over a greater area on the camera sensor. As a result, they are darker on average than less defocussed images.

¹The scattered intensity grows with the cross-section of the droplet

Figure 3.1: Overlapping defocussed droplet images

Minimum droplet size. Damaschke et al. [6] argue that the smallest measurable droplet is one that produces exactly one fringe covered by the aperture. We propose that, at least in theory, a partial fringe should be measurable if its image is sufficiently zero-padded before the Fourier transform is applied to it. *This might need elaboration.* In practice, the intensity of scattered light is likely to drop below an acceptable level before the fringes become too large, and noise (see above) will become the overwhelming problem. The researcher should also be aware that the assumptions of geometric optics that underlie (3.2) do not hold for small droplets (see Section 3.5 for details).

3.2 Setup

(How it's set up, what cameras, what lenses, what laser, timer box, software, etc.)

3.3 Common problems and sources of error

3.3.1 Too much overlap

This is a section where I refer to the paper that calculates overlap probabilities. I explain that many droplets are mis-identified (either high-freq is seen as low-freq, or noise is seen as high-freq) and where I point out that while Hanning windows and min-distance/max-overlap filters help a little bit, they also skew the representativeness of the sample because only small, dispersed satellites are outside of the main flow.

I explain that there isn't really an easy method of fixing this, and that any time spent attempting to deal with the problem is better spent building a slit aperture system, as described in the next chapter.

3.3.2 Droplet detection and camera mapping

The most challenging stage of the measurement process is the detection of the defocussed droplet images. Since the defocussed images assume the shape of the aperture, which is wide open in most applications,² they are typically circular. Moreover, they are all more or less of the same size as a consequence of equation (??).

It thus stands to reason that a simple circle detection technique would suffice to detect the droplet images in the photos. A polar adaptation of the Hough accumulator technique (such as the OpenCV implementation `cv2.HoughCircles()`) or a correlation-based pattern matching method (e.g. `cv2.matchTemplate()`) are both obvious choices for this task. The problem of *droplet overlap*, however, can thwart such efforts (Figure 3.1). This happens particularly when large droplets are to be measured, because their many fringes

²see Chapter ?? for a discussion of the benefits of non-circular apertures.

require larger defocussed images to resolve clearly. Indeed, in regions of high droplet density, it can be impossible to reliably detect the circular fringe images using the methods mentioned above.

Nevertheless, once droplet image positions are established with confidence, overlap can be dealt with to a degree: known overlapping regions can either be excluded entirely or serve to help find maximum-likelihood frequency peaks for their respective tributary droplet images.

Since the detection of droplet images is so essential, the Dantec DynamicStudio software extracts the droplets' positions from the focussed photo, and then maps those positions onto the defocussed photo based on a set of camera calibration photos. This method is sound in principle, but often yields unsatisfactory mappings in practice, likely whenever the calibration target plate (Figure ??) is not precisely aligned with the laser sheet. In Section ??, we describe a more accurate and robust method of finding the mapping based directly on the pair of droplet photos.

Since the mapping error is often a perspectivity, the simple manual x/y -shift that can be applied in the DynamicStudio software after calibration is not a sufficient adjustment.

Dantec supplies a *standard dot target*, a white $10 \times 10 \text{ cm}^2$ plate engraved with a pattern of black dots (Figure ??). The plate is to be mounted such that its surface coincides perfectly with the laser sheet. Both cameras are then focussed on the dot pattern, and a photo is taken with both. This allows the DynamicStudio software to calculate the transformation matrix between target plate and image for each camera:

$$\begin{bmatrix} x' \\ y' \\ z' \\ r' \end{bmatrix} = \begin{bmatrix} S_x & A_{yx} & A_{zx} & T_x \\ A_{xy} & S_y & A_{zy} & T_y \\ A_{xz} & A_{xy} & S_z & T_z \\ P_x & P_y & P_z & S_0 \end{bmatrix} \begin{bmatrix} x \\ y \\ z \\ 1 \end{bmatrix}. \quad (3.4)$$

In practice, $P_{x,y,z} = 0$ and $S_z = S_0 = 1$, such that the mapping is affine (although we will later show that this need not be the case). The z -components (third row/column) are ignored, such that a 3×3 matrix suffices for the purposes of this discussion:

$$\begin{bmatrix} x' \\ y' \\ r' \end{bmatrix} = \begin{bmatrix} S_x & A_{yx} & T_x \\ A_{xy} & S_y & T_y \\ P_x & P_y & S_0 \end{bmatrix} \begin{bmatrix} x \\ y \\ 1 \end{bmatrix}. \quad (3.5)$$

The DynamicStudio software thus finds the camera matrices \mathbf{P}_{foc} and \mathbf{P}_{def} mapping the object (the target plate) onto the two camera images:³

$$\mathbf{x}'_{\text{foc}} = \mathbf{P}_{\text{foc}} \mathbf{x} \quad (3.6)$$

$$\mathbf{x}'_{\text{def}} = \mathbf{P}_{\text{def}} \mathbf{x}. \quad (3.7)$$

It follows that the quotient of the two matrices, also known as the homography

$$\mathbf{H} = \mathbf{P}_{\text{def}} \mathbf{P}_{\text{foc}} \quad (3.8)$$

³Henceforth, the subscripts "foc" and "def" shall designate the focussed and defocussed cameras, respectively – even though both are focussed when the initial calibration photo is taken.

can be used to map the focussed image onto the defocussed image:

$$\mathbf{H} \mathbf{x}'_{\text{foc}} = \mathbf{x}'_{\text{def}}. \quad (3.9)$$

In practice, it is not always possible to ensure that the dot target plate is aligned with the laser light sheet to absolute perfection. This introduces a perspective error in the homography matrix \mathbf{H} . Figure 3.2a shows that even though the calibration images are mapped perfectly, there is a perspective error in Figure 3.2b.

To correct for this error, we can use image registration techniques to derive the homography mapping *directly* from the focussed and defocussed droplet images, doing away with the need for calibration pictures altogether. Once we find the corrected homography $\hat{\mathbf{H}}$, we use it to find

$$\hat{\mathbf{P}}_{\text{def}} = \hat{\mathbf{H}} \mathbf{P}_{\text{foc}}, \quad (3.10)$$

which can be manually entered into the DynamicStudio software to replace \mathbf{P}_{def} .

Finding the corrected homography

Image registration is the process of finding the best possible mapping of one image onto another – in other words, it is a term for homography-finding techniques. The basic process comprises three steps:

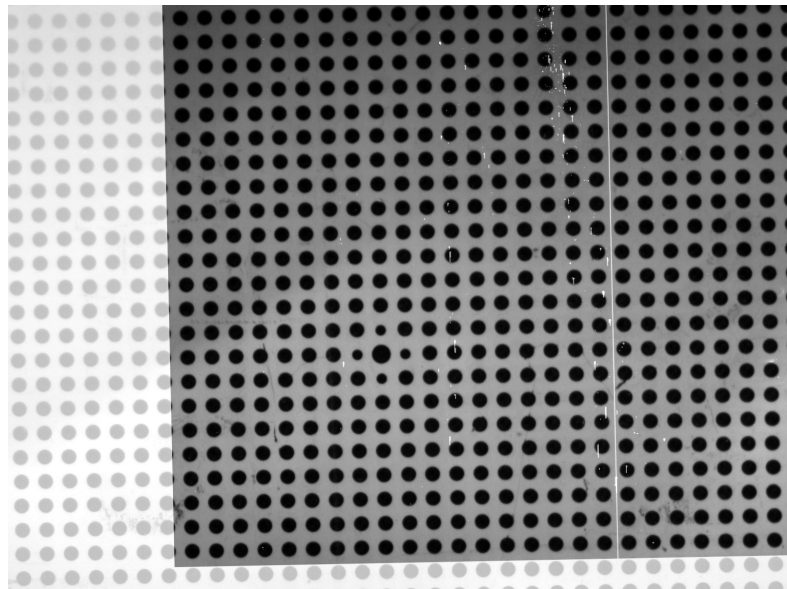
1. **Feature detection:** Finding “features”, i.e. unique points or regions in the images – such as corners, arcs, or contrasting regions which stay relatively stable even when the image is thresholded.
2. **Feature description:** Converting the detected features into numerical vectors.
3. **Feature matching:** Finding good correspondences between features in the two images – this often requires inlier/outlier decision-making, e.g. RANSAC.

Naturally, image registration is impossible to achieve between our focussed and defocussed images. We therefore first apply the following steps to our focussed image:

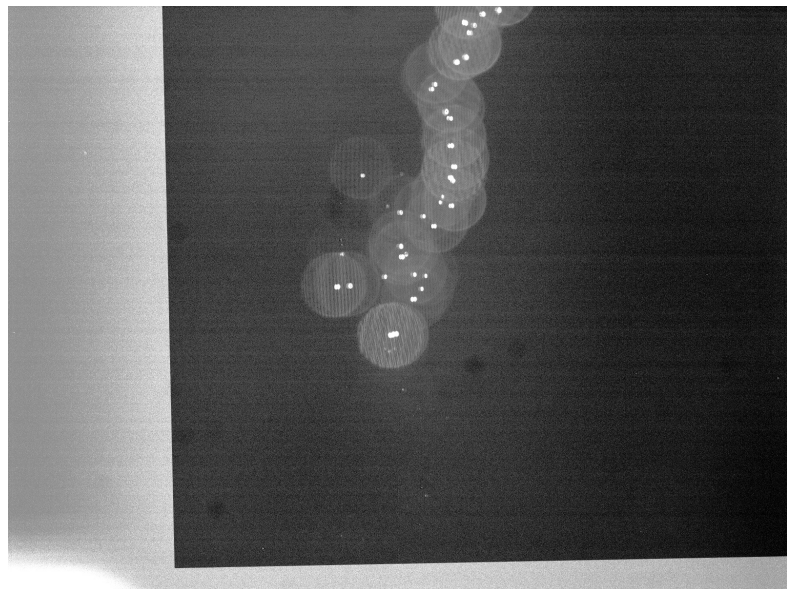
1. Mask the image, excluding all areas that are known not to contain droplets.
2. Subtract the pixel-wise minimum or mean taken over all images taken by the camera. This step will remove hot pixels on the camera’s CCD sensor and other static noise.
3. Erode the image, using a 3×3 or 5×5 kernel. This will close any remaining bright pixels which are likely noise.
4. Locate the intensity peaks in the remaining image.
5. Fill a new image with black, then draw white circles of diameter D_d onto it, centered at the respective positions of the intensity peaks detected in the focussed image.

The result of these operations is shown in Figure 3.3.

Image registration algorithms are often not very robust. This is especially true when the two pictures are not photos taken from slightly different angles. Moreover, image processing algorithms have runtime complexities that grow at least with the area of the image.



(a) Focussed camera image, after applying homography, is superimposed onto defocussed camera image of dot target plate.

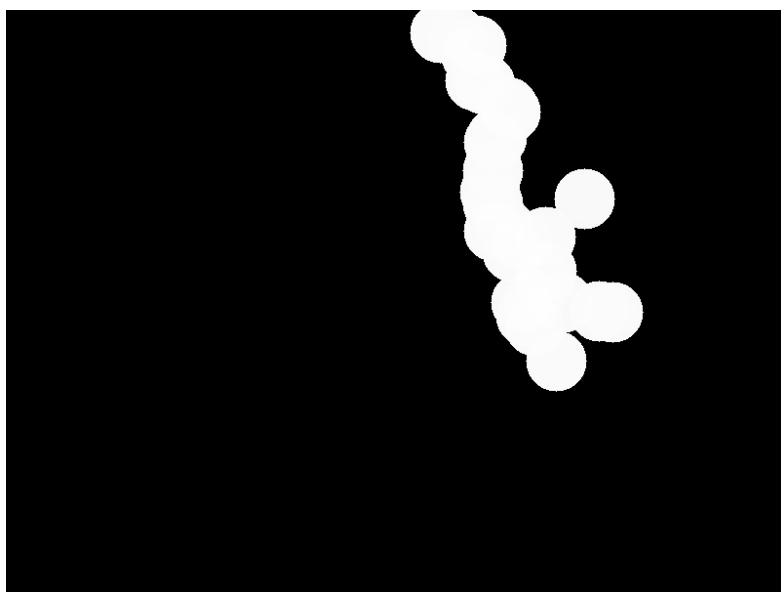


(b) Focussed camera image, after applying homography derived from the calibration images, is superimposed onto defocussed camera image of droplets.

Figure 3.2: Illustration of the perspective error from misaligned calibration target plate



(a) Focussed camera image.



(b) Simulated defocussed camera image based on focussed camera image,
used for registration.

Figure 3.3: Using the focussed image to simulate the defocussed image for registration

We therefore prepare our focussed image by shrinking it to half the size (transformation $\mathbf{S}_{0.5}$) and mirroring it horizontally (transformation \mathbf{M}_h).

Our image registration algorithm makes use of the affine invariance of the ASIFT algorithm [1], but instead of the patented SIFT detector/descriptor pair [2], we use ORB [3] for feature detection and BRIEF [4] for feature description. A more detailed explanation of the algorithm can be found in Appendix ???. Figure 3.4 shows a successful mapping between focussed and defocussed images.

The homography found by the registration algorithm, \mathbf{K} , must now be converted into a homography between the original images, $\hat{\mathbf{H}}$. We see that

$$\mathbf{K} \mathbf{M}_h \mathbf{S}_{0.5} \mathbf{P}_{\text{foc}} = \mathbf{S}_{0.5} \mathbf{P}_{\text{def}}; \quad (3.11)$$

note here that the mirroring operation is applied only on one side of the equation, since the original images are mirrored and the goal is to undo this before running the image registration. To bring this into the form required by (3.9), we write

$$\mathbf{S}_{0.5}^{-1} \mathbf{K} \mathbf{M}_h \mathbf{S}_{0.5} \mathbf{P}_{\text{foc}} = \mathbf{S}_{0.5}^{-1} \mathbf{S}_{0.5} \mathbf{P}_{\text{def}} \quad (3.12)$$

$$= \mathbf{P}_{\text{def}} \quad (3.13)$$

Finally, it turns out that DynamicStudio violates convention by placing the coordinate origin at the bottom left corner of the image. We must therefore pre- and post-multiply by $\mathbf{M}_v^{\pm 1}$ to arrive at our final expression for $\hat{\mathbf{H}}$:

$$\hat{\mathbf{H}} = \mathbf{M}_v \mathbf{S}_{0.5}^{-1} \mathbf{K} \mathbf{M}_h \mathbf{S}_{0.5} \mathbf{M}_v^{-1}. \quad (3.14)$$

We shall provide the transformation matrices for convenience:

$$\mathbf{M}_h = \begin{bmatrix} -1 & 0 & (\text{image width}) \\ 0 & 1 & 0 \\ 0 & 0 & 1 \end{bmatrix} \quad (3.15)$$

$$\mathbf{M}_v = \begin{bmatrix} 1 & 0 & 0 \\ 0 & -1 & (\text{image height}) \\ 0 & 0 & 1 \end{bmatrix} \quad (3.16)$$

$$\mathbf{S}_{0.5} = \begin{bmatrix} 0.5 & 0 & 0 \\ 0 & 0.5 & 0 \\ 0 & 0 & 1 \end{bmatrix} \quad (3.17)$$

The improved matching achieved using $\hat{\mathbf{P}}_{\text{def}}$ is shown in Figure 3.5. Having calculated $\hat{\mathbf{P}}_{\text{def}}$ using equation (3.10), we can import it into DynamicStudio to improve the identification of droplets.

3.4 Thin lens assumption

What matters is the Numerical Aperture (NA), which is (the sine of half of) the collection angle. When we have a simple lens, we can calculate this as

$$\text{NA} = \sin \frac{d_a}{2z} 3\alpha\rho = \sqrt{2\lambda xr} \quad (3.18)$$

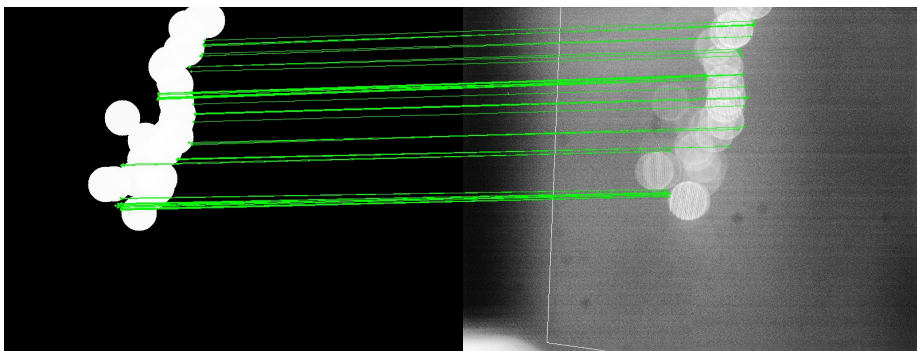


Figure 3.4: Matching between focussed and defocussed images.

The Dantec manual suggests using the distance from light sheet to front of the lens for z , and the ratio of min focal length and max f-number to find d_a . This, however, does not result in an accurate value for the collection angle with all lenses.

We are assuming, then, that the effective aperture (the entrance pupil) always stays constant throughout the focussing range of the lens. This is not necessarily the case, as there are lenses which change both the physical and the virtual size of the aperture when focussing. The best way to get the collecting angle is to go by magnification

3.4.1 Finding the correct value for aperture diameter

Here is where I make the claim that it is impossible to determine the actual exact value for the numerical aperture of the lens. Similarly, it can be quite difficult to determine the accurate distance from light sheet to lens aperture (even though the latter measurement is more forgiving, since the distances are far greater).

3.5 Error in the Mie approximation at small sizes

As outlined in paper ... geometric optics deviate from the true Mie scattering field when sizes are very small.

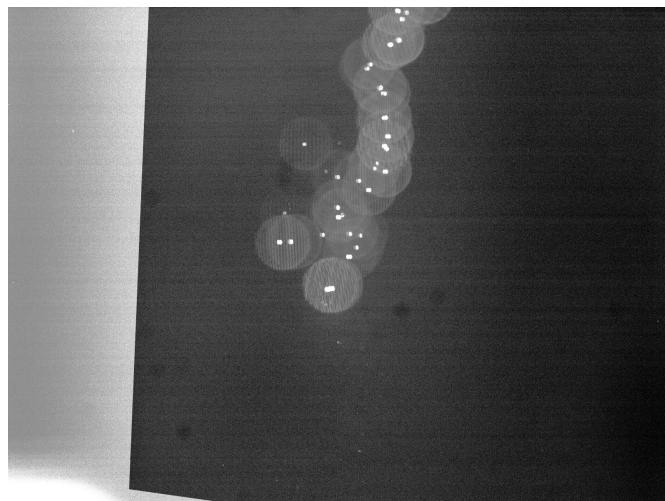


Figure 3.5: Focussed camera image, after applying homography derived from image registration, is superimposed onto defocussed camera image of droplets.

Particle sizing with a slit aperture

As we discussed in Section 3.3.1, many otherwise well-executed IPI measurements are thwarted by overlapping defocussed droplet images. This problem is never more apparent than in efforts to calibrate the system using a vibrating orifice droplet generator, as the droplets produced thereby are spaced very closely and produce heavily overlapping defocussed images. Fortunately, there exists a simple and reliable technique to deal with this problem: a slit aperture, installed directly in front of the lens, masks the defocussed droplet images such that only a thin strip across their center passes through the lens. The effect is shown in Figure 4.1.

The idea of optically compressing an image in one direction is well-known from the field of spectroscopy. It was first introduced to the area of fluid measurement by Durst et al. [7], and has since been employed in various forms, e.g. by Pan et al. [2]. Other authors use cylindrical lenses instead of slit apertures to achieve the vertical integration of the image [4].

4.1 The slit aperture

Naturally, equations (3.2) and (3.3) still hold.

(Insert a diagram of the setup)

(Describe how an aperture can be created in any lab)

(Show a picture of the lens with aperture)

4.2 Image processing

Extracting the fringe counts from such an image is straightforward. First, we correlate the image with that of a single, solid bright rectangle which shares the approximate dimensions of a typical strip in the image. This operation yields intensity peaks centered over our regions of interest. We remove closely adjacent peaks, as they may represent questionable or overlapping strips. Compared to the sheer number of correctly identified strips, the

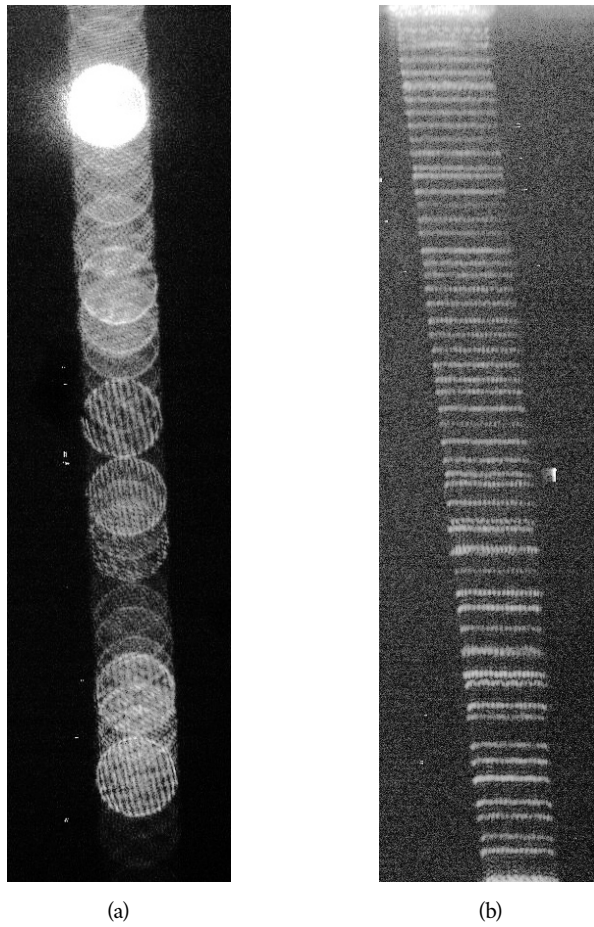


Figure 4.1: Before (a) and after (b) installing the slit aperture. The aperture stop pares off the top and bottom halves of the defocussed circles, leaving only a narrow center string in the middle.

number of legitimate data points lost this way is negligible. Figure 4.2 shows the result of such an attempt at identifying the strips.

To find the number of fringes within the strip, we cannot rely on counting the number of dark/bright variations directly, as some of them may be lost in the noise. The spatial frequency of the peaks, however, taken together with the known and constant horizontal width of the strips, will produce a reliable fringe count. In the next step, our algorithm therefore applies the Fourier transform to each region of interest. To improve the accuracy of the method, three steps are performed before the Fourier transform is taken:

1. a weak (3×3) Gaussian blur is applied to the region (optional);
2. a Hanning window is applied to the region – both horizontally and vertically. This

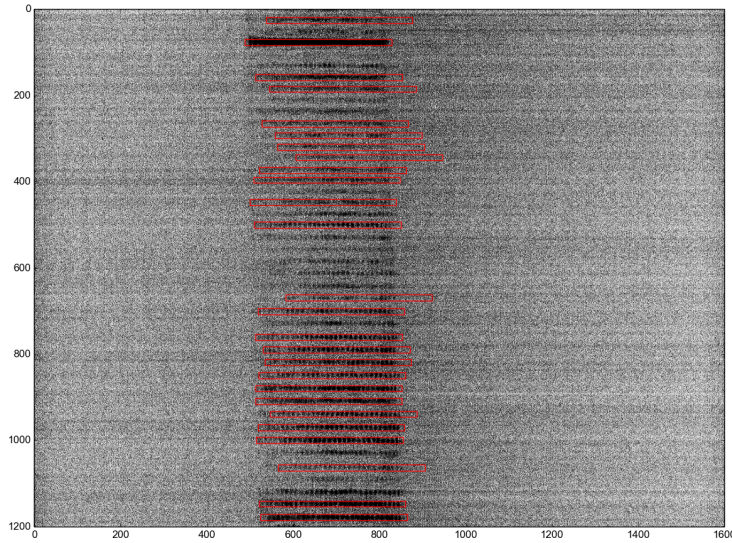


Figure 4.2: The image is correlated with that of a solid bright rectangle, which results in peaks that approximately coincide with the centres of the strips. Here, the original photo is shown with rectangles drawn centered at said peaks.

reduces the “sinc ringing” effect encountered when taking the Fourier transform of finite signals;

3. the region is padded with zeros in all directions to yield a larger input to the Fourier transform. In our application, the windowed and padded strip images had dimensions of 1024×1024 pixels. Zero-padding increases the granularity of the frequency spectrum, which can help with the correct identification of the peak frequency.

Figure 4.3 shows the windowed appearance of one such region of interest (although it does not show the padded input to the Fourier transform due to space constraints). The Fourier transform yields a frequency power spectrum in two dimensions, although we are primarily interested in the frequency peak in the horizontal direction (i.e. along $y = 0$). In order to minimize the misidentification of dominant frequencies,

1. we clip the spectrum to a band of reasonable frequencies. This is necessary because a) $1/f$ -noise causes very low frequencies to dominate in power, although they are of no interest to us, and b) graininess in the original photo can sometimes result in meritless high-frequency peaks;
2. we apply a Gaussian blur to the 2D spectrum to remove outliers in the spectrum;
3. we discard all regions in which the peak frequency’s power does not exceed a certain value;
4. we discard all regions in which the *prominence* of the peak frequency’s power (i.e. its proportion to the mean power) does not exceed a certain value (this step is optional).

The bottom two elements in Figure 4.3 illustrate the effect of these steps.

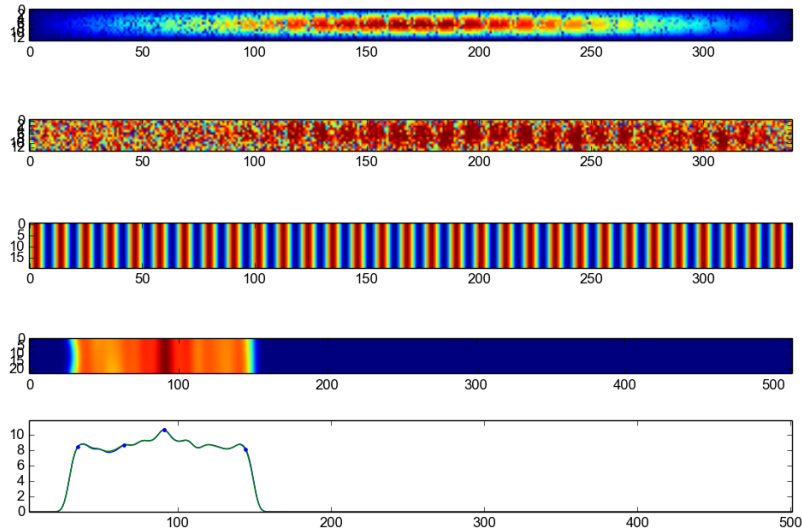


Figure 4.3: From top to bottom: windowed region of interest; original (unwindowed) region of interest; sine wave representing the identified peak frequency; clipped and lowpass-filtered 2D frequency spectrum showing a distinct peak at about 90 oscillations across the image width of 1024 pixels; 1D plot of the frequency spectrum, with peak identified at $f = 91.0$.

Finally, the peak frequency f_{peak} is converted into a fringe count by re-scaling it from the padded size D_{padded} (= 1024 pixels) to the width of the strip (which, in the context of IPI measurements, should equal the diameter D_i of the defocussed droplet image):

$$N_{\text{fr}} = f_{\text{peak}} \frac{D_i}{D_{\text{padded}}} \quad (4.1)$$

In the current implementation of our algorithm, D_i must be determined and entered manually.

4.3 Sources of error with the slit method

4.3.1 Misalignment of slit and lens

While the above algorithm will generally give a good estimate of the fringe count for a given defocussed droplet image, it cannot know whether the entire center portion of the image has indeed passed the slit aperture. It is conceivable, after all, that the slit aperture was not perfectly centered

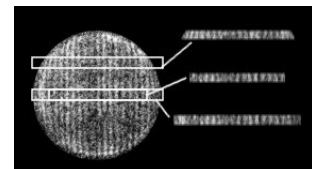


Figure 4.4: Only a slit aperture centered on the lens and extending across the entire lens entrance will preserve all fringes

on the lens entrance, or that the slit aperture was shorter than the diameter of the lens entrance. Figure 4.4 illustrates how the slit aperture can cause the defocussed image to appear smaller than it is. The reduced value for D_i , manually entered in equation (4.1), will result in droplets being reported as smaller than they are in reality.

4.4 Calibrating the slit method

Taking into account the sources of errors explained in the sections above, it is advisable to run a few calibration tests with droplets of different sizes before employing the IPI technique for real spray measurements. Recall that, if we ignore the Mie error (Section 3.5), the relationship between fringe count and droplet diameter is linear with a constant of proportionality χ (see equation (3.2)). The aim of our calibration, then, is to determine the value of χ from experiment – the premise being that we cannot be certain of the values of D_a , z , and possibly not even m and φ (although the latter can usually be ascertained to a sufficient degree of accuracy).

4.4.1 A sample calibration of the slit aperture method

Using the droplet generator described in Section 2.3 and the IPI configuration described in Section 3.2, we produced and measured monodisperse droplets of many different diameters. The droplet diameters were determined both mathematically and photographically, as described in Section ???. Out of over 30 sets of IPI measurements we selected six sets that exhibited both strong uniformity and high photographic quality:

Set	Flow rate	Frequency	D_d , predicted	D_d , from photo	\hat{N}_{fr}
FA	20.8 ml/h	5395 Hz	127 μm	126 μm	9.71
FB	39.7 ml/h	1990 Hz	220 μm	226 μm	16.71
FC	79.4 ml/h	1565 Hz	299 μm	291 μm	22.92
FD	94.3 ml/h	1067 Hz	361 μm	367 μm	27.26
FE	114.1 ml/h	1065 Hz	384 μm	384 μm	29.89
FF	175.2 ml/h	1038 Hz	447 μm	454 μm	34.56

Table 4.1: Six sets of calibration data taken with the setup described in Section 3.2

The values for \hat{N}_{fr} , the peak fringe count, are based on the histograms (see Figure 4.5) showing the distribution of fringe counts within each dataset. These fringe counts are of course found by the algorithm described in Section 4.2.

It is worthwhile to point out some apparent idiosyncrasies in the histograms of datasets FB and FC. Their peak fringe counts are 16.71 and 22.92, but there are secondary peaks at about 21 and 29 fringes, respectively. The latter are explained by the collision of droplets as discussed in Section 2.4.1, and are ignored for the purposes of calibration.

The close agreement of the droplet diameters found from photographs with those predicted by (??) reassures us that we can use the predicted D_d for further analysis.

At this point, we can least-squares-fit the linear relationship (3.2) to the primary peaks \hat{N}_{fr} and the known droplet diameters D_d to find \hat{x} :

$$\hat{x} = \frac{\sum_i D_{d,i} \hat{N}_{fr,i}}{\sum_i D_{d,i}^2} \quad (4.2)$$

Note that instead of the standard least squares regression we here use a simplified formula to force the trend line through the origin. This choice should not be made lightly, since it will usually cause the residuals to have a non-zero mean. In this case, however, we believe it to be justified to require that $D_d = 0$ for $N_{fr} = 0$.

Based on the values in Table 4.1, we thus arrive at a value of $\hat{x} = 76808.1$ with an R^2 -value of 99.98%.

4.4.2 Discussion

Figure 4.6 illustrates the good agreement on x between all datasets. Considering the sheer number of error sources – from the unavoidable non-uniformity of the generated droplets to the uncertainty that comes with taking the Fourier transform of a noisy image – the calibration results documented here are a testament to the practical robustness of the method.

It must be remembered, of course, that the peak fringe count values \hat{N}_{fr} forming the basis of our calculation are taken from the peaks of Gaussians fitted to the raw fringe count histograms (see Figure 4.5). In other words, it is our assumption that all droplets from a given dataset produce fringe counts that are normally distributed around their respective \hat{N}_{fr} . The histogram to dataset FA shows a much higher deviation than the others – this may be due to genuine variance in the generated droplet diameters or to difficulty in processing comparatively weak images with low fringe counts. It seems likely that both effects contribute.

We can compare the empirically determined value \hat{x} with the mathematical result obtained from (3.2). Substituting $\lambda = 532$ nm, $m = 1.3324$ and $\varphi = 90^\circ$, we conclude that

$$\frac{D_a}{z} = 2 \sin \left(\frac{\hat{x} \lambda}{\cos \frac{\varphi}{2} - \frac{m \sin \frac{\varphi}{2}}{\sqrt{m^2 + 1 - 2m \cos \frac{\varphi}{2}}}} \right) = 2 \sin(3.11982 \cdot 10^{-7} \hat{x}) \quad (4.3)$$

so for $\hat{x} = 76808.1$, $\frac{D_a}{z} = 0.047921$. Recall that this quotient is a measure of the collection angle and closely related to the numerical aperture $NA = \sin \frac{D_a}{2z}$. If needed, we can now use this result to compute the input parameters D_a and z in the DantecStudio IPI software: given, for instance, $z = 45.0$ cm, we can obtain the entrance pupil diameter as

$$0.047921 \cdot 450 \text{ mm} = 2.156 \text{ mm} \quad (4.4)$$

4.5 Conclusion

- It's impossible to calibrate IPI using a VOAG

- The slit aperture works pretty well
- Calibration is easy, and one or two calibrations are probably enough
- A good collection angle (i.e. camera-laser distance) must be chosen

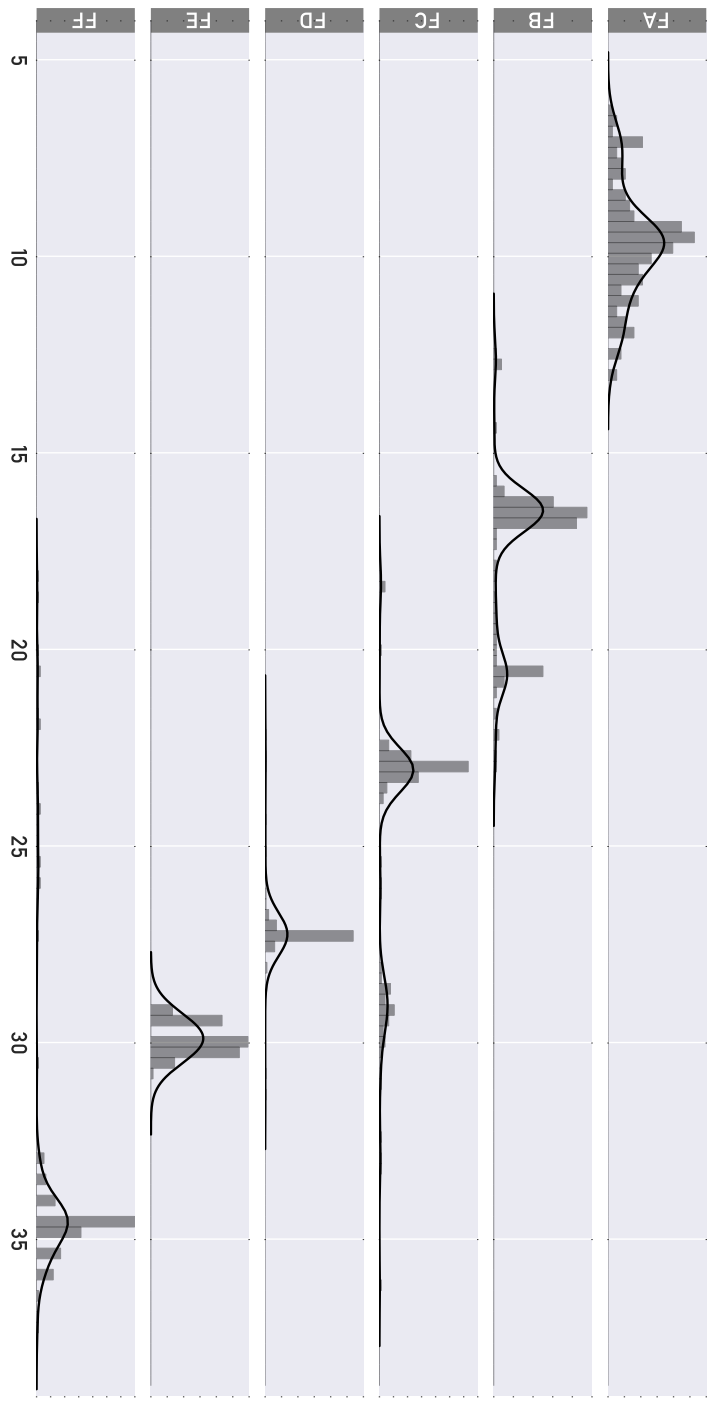


Figure 4.5: Normalized distributions of measured fringe counts N_{fr} for the six datasets listed in Table 4.1. Solid lines are Gaussian kernel density estimates with $h = 0.5$.

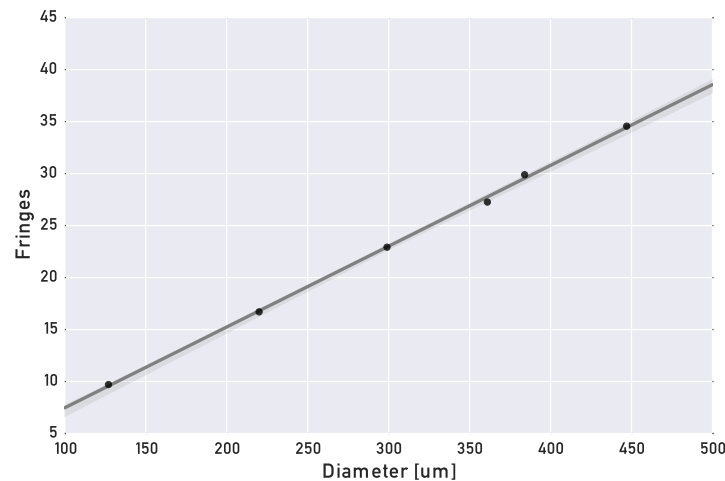


Figure 4.6: Scatterplot of Table 4.1 showing the peak fringe counts \hat{N}_{fr} for each predicted droplet diameter D_d

Phase-Doppler Particle Analysis (PDPA)

5.1 Optical principle

(Explanation)

5.2 Sources of error

5.2.1 Gaussian beam divergence

The theory predicting the linear relationship between detector phase difference and droplet diameter is founded on the assumption of very small droplets and plane beam wavefronts.
(Question: is it the wavefront curvature or the non-uniformity of the intensity that causes problems?)

The problem is termed *trajectory ambiguity effect* (TAE) or *Gaussian beam defect* (GBD) in the literature.

This phenomenon was recognized first by Saf [8] but had to be neglected until the plane-wave scattering theory of Lorenz-Mie optics was extended into the *Generalized Lorenz-Mie Theory* (GLMT). Most of this work was done by Gouesbet, Gréhan, Maheu, Lock and others throughout the 1980s [9, 10, 11, 12], and mathematically rigorous formulations were available by the early 1990s [13, 14]. The 1996 paper by Gouesbet and Gréhan summarizes these developments and provides an early overview over the attempts to circumvent the TAE [15]. More discussion is given e.g. by

Solutions are a) a planar setup, b) double-burst measurements, c) epsilon validity measurements. It is important to align the receiver properly; the tables used by TSI were developed using GLMT by Naq [16].

5.2.2 Slit effect

Durst et al show experimentally that the slit effect is even more crucial than the Gaussian beam effect. [7]. Together with the TAE, this is called the measurement volume effect. Qiu

and Hsu propose using four detectors, instead of three, to resolve this problem entirely [17]. A similar design was verified experimentally by Sipperley and Bachalo [18].

A more recent review of the phenomenon and associated techniques was given by Strakey et al. [19?].

5.2.3 Change in fringe frequency over z

The curved wavefront causes the fringe spacing to vary along the axis of the measurement volume. At the near and far ends of the volume, the fringes are spaced wider, which can result in an error on the order of 10%. (Red Book)

5.2.4 Selection of lenses and masks

Davis and Disimile talk about the TAE only tangentially. They provide results of the same spray using different masks and focal lengths [20].

5.2.5 Wrongly entered parameters

The optical principle involves many more geometric parameters than are needed for the operation of IPI or laser diffraction (Malvern) devices. As a result, an excellent interface and a very attentive user are required to ensure accurate results.

5.3 Calibration

Calibration is easy in theory:

1. Calibrate for inherent phase difference using calibration diode
2. Set up monodisperse spray
3. Set up optical parameters in software
4. Take measurement; use coincidence; turn up PMT so that the top intensities saturate just barely
5. (Optional) Apply validation somehow
6. Use calibration window to determine detector separation values
7. Done!

In practice, I always get error messages when doing the last step, and the values are way out of the expected range. The result, then, is that the D20 is made very close to the expected monodisperse diameter. Since the D20 is quite a bit larger than the actual (and completely obvious) peak value, even these "wrong" values aren't correct.

TODO: Find out if it's the optical parameters that are wrong, or if something else is missing.

Bibliography

- [1] A. R. Glover, S. M. Skippon, and R. D. Boyle. Interferometric laser imaging for droplet sizing: a method for droplet-size measurement in sparse spray systems. *Appl Opt*, 34: 8409–8421, Dec 1995.
- [2] G. Pan, J. Shakal, W. Lai, R. Calabria, P. Massoli, and O. Pust. Simultaneous global size and velocity measurement of droplets and sprays. *Spray '06 – Workshop über Sprays, Erfassung von Sprühvorgängen und Techniken der Fluidzerstäubung*, 2006.
- [3] H. van de Hulst. *Light Scattering by Small Particles*. Dover Books on Physics. Dover Publications, 2012. ISBN 9780486139753. URL <http://books.google.ca/books?id=P1HfPMVAFRcC>.
- [4] T. Kawaguchi, Y. Akasaka, and M. Maeda. Size measurements of droplets and bubbles by advanced interferometric laser imaging technique. *Meas Sci Technol*, 13:308–316, Feb 2002.
- [5] C. Mounaïm-Rousselle and O. Pajot. Droplet sizing by mie scattering interferometry in a spark ignition engine. *Part Part Syst Charact*, 16:160–168, 1999.
- [6] N. Damaschke, H. Nobach, and C. Tropea. Optical limits of particle concentration for multi-dimensional particle sizing techniques in fluid mechanics. *Experiments in Fluids*, 32:143–152, 2002.
- [7] F. Durst, C. Tropea, and T.-H. Xu. The slit effect in phase doppler anemometry. Oct 1994.
- [8] The use of polarized light for optical particle sizing. In *Proceedings of the 3rd International Symposium on Applications of Laser Anemometry to Fluid Mechanics, Lisbon, Portugal*, page 18.2, 1986.
- [9] G. Gréhan, G. Gouesbet, and C. Rabasse. The computer program supermidi for lorenz-mie theory and the research of one-to-one relationships for particle sizing. In *Proceedings of the symposium on long range and short range optical velocity measurements*, Institut franco-allemand de Saint-Louis, September 1980.
- [10] G. Gouesbet and G. Gréhan. Sur la généralisation de la théorie de lorenz-mie. *Journal of Optics*, 13(2):97–103, 1982.

- [11] Light scattering from a sphere arbitrarily located in a gaussian beam, using a bromwich formulation. *Journal of the Optical Society of America A*.
- [12] B. Maheu, G. Gouesbet, and G. Gréhan. A concise presentation of the generalized lorenz-mie theory for arbitrary location of the scatterer in an arbitrary incident profile. *Journal of Optics*, 19(2):59–67, 1988.
- [13] J. A. Lock and G. Gouesbet. A rigorous justification of the localized approximation to the beam shape coefficients in generalized lorenz-mie theory, i. on-axis beams. *Journal of the Optical Society of America A*, 11(9):2503–2515, 1994.
- [14] G. Gouesbet and J. A. Lock. A rigorous justification of the localized approximation to the beam shape coefficients in generalized lorenz-mie theory, ii. off-axis beams. *Journal of the Optical Society of America A*, 11(9):2516–2525, 1994.
- [15] G. Gouesbet and G. Gréhan. Gaussian beam errors in phase-doppler anemometry and their elimination. In R. Adrian, D. Durão, F. Durst, M. Heitor, M. Maeda, and J. Whitelaw, editors, *Developments in Laser Techniques and Applications to Fluid Mechanics*, pages 243–259. Springer Berlin Heidelberg, 1996.
- [16] A rigorous procedure for design and response determination of phase doppler systems. In *Proceedings of the 7^h International Symposium on Applications of Laser Anemometry to Fluid Mechanics, Lisbon, Portugal*, pages 340–353, 1994.
- [17] H. Qiu and C. T. Hsu. Method of phase-doppler anemometry free from the measurement-volume effect. *Applied Optics*, 38(13):2737–2742, May 1999.
- [18] C. M. Sipperley and W. D. Bachalo. Triple interval phase doppler interferometry: Improved dense sprays measurements and enhanced phase discrimination. In *17^h International Symposium on Applications of Laser Techniques to Fluid Mechanics, Lisbon, Portugal*, Jul 2014.
- [19] P. A. Strakey, D. G. Talley, S. V. Sankar, and W. D. Bachalo. Phase doppler interferometry with probe-to-droplet size ratios less than unity. part i: Trajectory errors. *Applied Optics*, 39(22):3875–3886, Aug 2000.
- [20] J. M. Davis and P. J. Disimile. The effect of optical configuration selection on phase doppler anemometer fire suppressant nozzle characterizations. In *14th Halon Options Technical Working Conference*, May 2004.